Applied Surface Science 393 (2017) 93–102

Contents lists available at ScienceDirect

Applied Surface Science

journal homepage: www.elsevier.com/locate/apsusc

Full length article

Enhancing performance and surface antifouling properties of polysulfone ultrafiltration membranes with salicylate-alumoxane nanoparticles

Samaneh Mokhtari [a], Ahmad Rahimpour [a,*], Ahmad Arabi Shamsabadi [b], Setareh Habibzadeh [c], Masoud Soroush [b,*]

[a] Membrane Research Center, School of Chemical Engineering, Babol University of Technology, Babol, Iran
[b] Department of Chemical and Biological Engineering, Drexel University, Philadelphia, PA 19104, USA
[c] Faculty of Basic Science, Department of Chemistry, Babol University of Technology, Babol, Iran

ARTICLE INFO

Article history:
Received 26 May 2016
Received in revised form 2 September 2016
Accepted 2 October 2016
Available online 3 October 2016

Keywords:
Salicylate-alumoxane nanoparticles
PS ultrafiltration membranes
Surface hydrophilicity
Surface antifouling properties

ABSTRACT

To improve the hydrophilicity and antifouling properties of polysulfone (PS) ultrafiltration membranes, we studied the use of salicylate-alumoxane (SA) nanoparticles as a novel hydrophilic additive. The effects of SA nanoparticles on the membrane characteristics and performance were investigated in terms of membrane structure, permeation flux, solute rejection, hydrophilicity, and antifouling ability. The new mixed-matrix membranes (MMMs) possess asymmetric structures. They have smaller finger-like pores and smoother surfaces than the neat PS membranes. The embedment of SA nanoparticles in the polymer matrix and the improvement of surface hydrophilicity were investigated. Ultrafiltration experiments indicated that the pure-water flux of the new MMMs initially increases with SA nanoparticles loading followed by a decrease at high loadings. Higher BSA solution flux was achieved for the MMMs compared to the neat PS membranes. Membranes with 1 wt.% SA nanoparticles exhibit the highest flux recovery ratio of 87% and the lowest irreversible fouling of 13%.

1. Introduction

Ultrafiltration (UF) is a membrane separation process driven by pressure difference [1,2]. It has been employed for the removal of various components such as macromolecules, proteins, and viruses from different solutions [3,4], in food processing, water and wastewater treatment and seawater desalination [5,6]. Low operating costs, high flux, satisfactory permeate quality, and simplicity are some advantages of UF over other membrane technologies [7,8].

The physical and chemical properties of polymers used in manufacturing UF membranes have strong effects on the structure and performance of the membranes [9,10]. Examples of such polymers are polysulfone (PS) [11], polyethersulfone (PES) [12], cellulose acetate (CA) [13], polyvinylidene fluoride (PVDF) [14], polyacrylonitrile (PAN) [15], polyethylene (PE), polypropylene (PP), and polyamide and polyimide [16]. Among these, PS is widely used due to its appealing physicochemical characteristics such as high thermal stability, adequate mechanical strength, high chemical resistance over a wide range of pH, and excellent film forming ability for UF applications [17,18]. However, a major disadvantage of PS is its hydrophobic nature, which causes membrane fouling [19,20]. Membrane fouling can be influenced by membrane characteristics, feed solution properties and operation conditions [21]. Typically, smooth and highly hydrophilic surfaces resist fouling [22]. Therefore, to improve membrane resistance against fouling, the surface hydrophilicity of the membrane should be improved [23]. Various methods have been applied to improve the surface hydrophilicity of UF membranes. Among them, incorporation of hydrophilic nanoparticles into polymer matrix is an effective way of providing membranes with adequate fouling resistance [24,25].

To prepare nanocomposite membranes, various nanoparticles such as titania (TiO_2) [26], mesoporous silica (SiO_2) [27], SiO_2–GO [28], alumina (Al_2O_3) [4], zirconia (ZrO_2) [29], zinc oxide (ZnO) [20], silver (Ag) [30], zeolite [31], and multi-walled carbon nanotubes [7,32] have been used. Arsuaga et al. [33] investigated the effect of metal oxide nanoparticles on the morphology and performance of nanocomposite membranes. They found that the presence of nanoparticles in the casting solution decreases contact angle, increases water flux, and improves fouling resistance. Vatanpour

* Corresponding authors.
E-mail addresses: ahmadrahimpour@yahoo.com, ahmadrahimpour@nit.ac.ir (A. Rahimpour), soroushm@drexel.edu (M. Soroush).

http://dx.doi.org/10.1016/j.apsusc.2016.10.005
0169-4332/

et al. [34] studied the antifouling properties of MMMs incorporated with boehmite nanoparticles. The addition of boehmite nanoparticles to the membranes changed the structure and morphology of the resulting membranes and created more hydrophilic and smoother surfaces, leading to a substantial increase in the solution flux and flux recovery ratio. While there have been many studies on modifying PSUF membranes using various hydrophilic nanoparticles, to best of our knowledge, there has been no reported study of using SA nanoparticles in the PS casting solution. SA nanoparticles form a stable inorganic material that is inexpensive, non-toxic, and resistant to chemical cleaning agents. Our expectation was that the addition of SA nanoparticles improves the hydrophilicity and surface properties, and decreases fouling of the MMMs due to the extra OH groups on their surfaces.

In this work, we aimed to fabricate novel PS/SA- UF membranes with satisfactory antifouling properties. To achieve this, we synthesized SA nanoparticles and loaded them into PS to fabricate high performance MMMs via the phase inversion method. Finally, the characteristics, structure, and morphology of the fabricated membranes were studied.

2. Materials and methods

2.1. Materials

Aluminum nitrate 9-hydrate [Al $(NO_3)_3{\cdot}9H_2O$] and sodium hydroxide (NaOH) supplied by Merck (Germany) and salicylic acid obtained from Scharlau (Germany) were used for the synthesis of boehmite and SA nanoparticles. Polysulfone (PS, Mw 35000 g/mol) provided by Solvay was used as the base polymer for the preparation of the mixed membranes. *N,N*-dimethylacetamide (DMAc, 99.8%) as the polymer solvent, Triton ×100 and sodium dodecyl sulfate (SDS) as surfactants, polyethyleneglycol (PEG) with a molecular weight of 400 Da as the pore former, and bovine serum albumin (BSA, MW ~66 kDa) as a model protein for fouling tests were purchased from Merck (Germany).

2.2. Preparation of boehmite nanoparticles

Boehmite nanoparticles were synthesized according to the procedure described in Ref. [35]. A brief summary of the procedure we used is as follows. First two solutions were made: a NaOH solution by dissolving 6.490 g of NaOH in 50 ml of distilled water, and an $Al(NO_3)_3{\cdot}9H_2O$ solution by dissolving 20 g of $Al(NO_3)_3{\cdot}9H_2O$ in 30 ml of distilled water. The sodium hydroxide solution was then gradually added to the Al $(NO_3)_3{\cdot}9H_2O$ solution at a rate of 2.94 ml/min, while the aluminum nitrate solution was stirred. The resulting milky solution was mixed and sonicated in an ultrasonic bath at 25 °C for 3 h. The mixture precipitate was then filtered out using a filter paper, washed with distilled water, and finally dried in an oven at 220 °C for 4 h.

2.3. Synthesis of salicylate alumoxane nanoparticles

Salicylate alumoxane (SA) nanoparticles were synthesized from the reaction between boehmite nanoparticles and salicylic acid using the procedure described next [36]. First, 6 g of boehmite nanoparticles and 12 g of salicylic acid were dissolved in 200 ml of distilled water. The resulting suspension was sonicated in the ultrasonic bath at 25 °C for 10 min and then refluxed at its boiling point. Next, the mixture was cooled to the room temperature, and filtered. To remove the unreacted salicylic acid, the precipitate was mixed with 200 ml of ethanol. The resulting mixture was filtered and kept in an oven at 60 °C. Fig. 1 shows the reactions involved in the deprotonation of salicylic acid and the production of salicylate alumoxane.

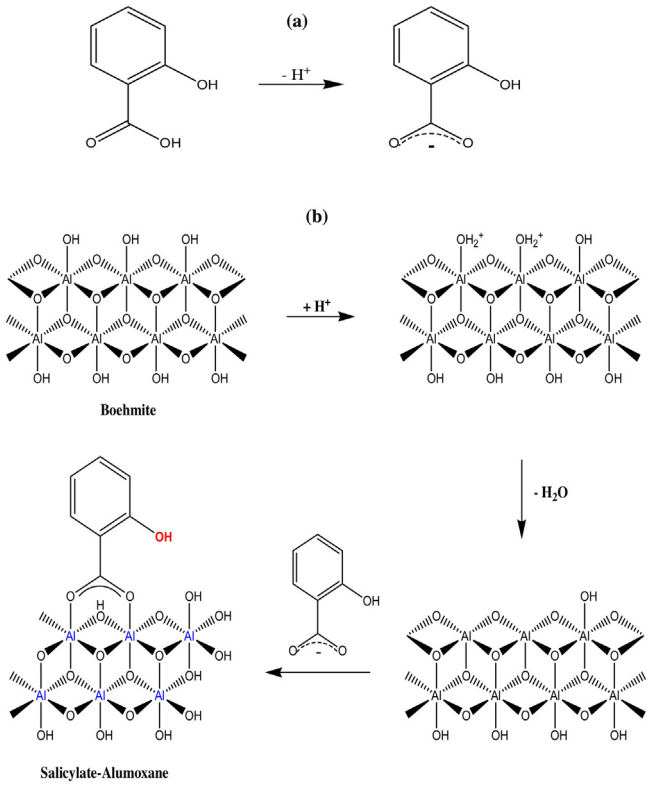

Fig. 1. (a) Deprotonation of salicylic acid and (b) reaction steps for the production of SA nanoparticles.

2.4. Preparation of SA/PS nanocomposite membranes

Neat and nanocomposite PS membranes were prepared using phase inversion induced by immersion precipitation. First, Triton X100 (2 wt.%) and PEG 400 (1 wt.%) were added to DMAc. Next, SA nanoparticles (0.1, 0.5, 1 and 2 wt.%) were added to three separate solutions and dispersed by an ultrasonic bath for 30 min. Triton X100 improves the dispersion of nanoparticles in the casting solution. After a complete dispersion of the nano fillers, the PS powder was added to the solution, and the mixture was stirred by a magnetic stirrer at 400 rpm for 12 h to form a uniform and homogeneous solution. Next, the polymer solution was kept motionless for 4 h to allow air bubbles to escape. The solution was then cast over a polyester non-woven fabric using a 75 μm-thick, casting knife and immediately immersed into a non-solvent bath containing distilled water and 0.1 wt.% SDS. SDS in the non-solvent bath influences the membrane morphology and performance. In particular, it improves membrane surface porosity and pore density, and consequently membrane permeability [37]. The fabricated membranes were washed with fresh distilled water several times to remove the residual solvent, followed by drying between two filter papers at room temperature. In this paper, we will call our membranes prepared with 0, 0.1, 0.5, 1 and 2 wt.% of SA nanoparticles UF-S0, UF-S0.1, UF-S0.5, UF-S1 and UF-S2, respectively.

2.5. Characterization of SA nanoparticles and membranes

To study the synthesized SA nanoparticles, transmission electron microscopy (TEM) (Zeiss – EM10C – 80 KV) was used. The thermal behavior of SA nanoparticles was investigated via thermogravimetric analysis (TGA-DCS1, Mettler-Toledo, S.A.E.) at a heating

rate of 10 °C/min up to 600 °C under nitrogen atmosphere. To measure the size and size distribution of SA nanoparticles, a particle size analyzer (Brookhaven, USA) was used. Sizes of the SA nanoparticles were measured using the dynamic light scattering (DLS) method. The FTIR spectrum of the boehmite, SA nanoparticles and ATR-IR spectra of PS/SA nanocomposite membranes were obtained using a FTIR-ATR spectrometer (Shimadzu Prestige-21, Japan) in a wave range of 400–4000 cm^{-1}. Hydrophilicity of the neat and nanocomposite PS membranes were determined by contact angle measurements made using a contact angle meter (OCA 15 plus, Dataphysics). The average of five measurements at different locations on each membrane surface was reported as the contact angle.

The top surface and cross-section areas of the prepared membranes were observed using a field emission scan electron microscope (FESEM, Philips-XL30, Netherlands) with an accelerating voltage of 3.0 kV. Prior to scanning, small pieces of the membrane samples were immersed into liquid nitrogen and then fractured to obtain a sharp cross section. The fractured samples were coated with a thin conductive layer of gold. Also, the EDAX analysis was used to confirm the presence of salicylate-alumoxane nanoparticles and their dispersion in the nanocomposite membranes.

Atomic force microscopy (AFM) images of prepared membranes were characterized using nanosurf AFM (Easyscan2 Flex) to improve the clarity of the surface roughness of the prepared membranes. The surface roughness parameters were expressed in terms of the average roughness (S_a), the root mean square of the Z data (S_q), and the mean difference between the five highest peaks and lowest valleys (S_z). The porosity of each membrane was determined by a gravimetric method; that is, calculating the weight of water in the membrane pores [38], and then using:

$$\varepsilon = \frac{\left(m_{wet} - m_{dry}\right)/\rho_w}{\left(m_{wet} - m_{dry}\right)/\rho_w + \left(m_{dry}/\rho_p\right)} \quad (1)$$

where m_{dry} and m_{wet} are the dry and wet masses of the membrane, respectively, ρ_w is the water density, and ρ_p is the polymer density.

The average pore size of the membranes was calculated using the experimental permeation data given elsewhere [38] and:

$$r_m = \sqrt{\frac{(2.9 - 1.75\varepsilon)8\mu l J}{\varepsilon \Delta P}} \quad (2)$$

where μ is the water viscosity (Pa s), l is the membrane thickness (m), J is the flux ($m^3\ h^{-1}\ m^{-2}$), and ΔP is the operational pressure (Pa).

2.6. Filtration experiments

The performance of the membranes was evaluated in terms of pure water flux, protein solution flux, and protein rejection. The permeation experiments of the UF membranes were carried out using a laboratory-scale stirred filtration cell at 3 bar and at room temperature. The membranes were compacted at a pressure of 3 bar for 1 h using distillated water to obtain a constant flux. After membrane compaction, the membrane flux was calculated using:

$$J = \frac{V}{At} \quad (3)$$

where V is the volume of permeate collected (L), A is the effective membrane area (m^2), and t is the collection time (h). Also, the BSA rejection was calculated using:

$$R = (1 - \frac{C_p}{C_f})100 \quad (4)$$

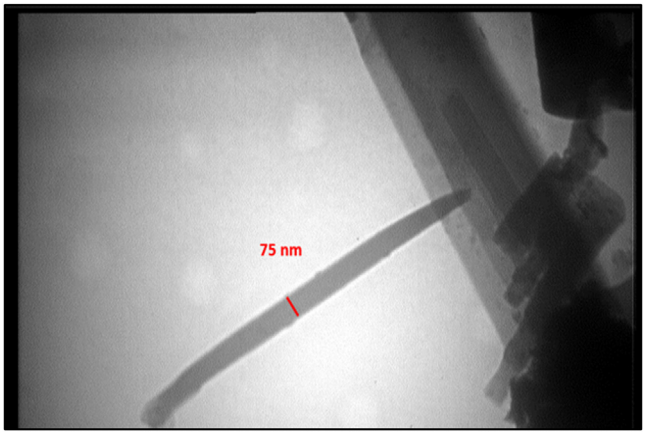

Fig. 2. TEM micrograph of the synthesized SA nanoparticles.

where C_p (mg/mL) and C_f (mg/mL) are the BSA contents in the permeate and feed solutions, respectively; these were measured using an UV-spectrophotometer at 280 nm wavelength.

2.7. Antifouling experiments

After making pure water flux measurements, the dead end cell was subjected to a 500 ppm BSA solution, and the BSA solution flux was calculated in 15 min intervals for 120 min. To reduce the influence of membrane concentration polarization, the rate of magnetic stirrer was set to 400 rpm. The feed concentration was kept constant by recycling the permeate stream to the cell. After 2 h of BSA filtration, the dead end cell was filled with 200 ml of distilled water at 40 °C under magnetic stirring at the rate of 600 rpm for 30 min. The pure water flux of the cleaned membranes (J_R) was measured again to calculate the flux recovery ratio (FRR) of the membranes using:

$$FRR = \left(\frac{J_{ww}}{J_{wi}}\right)100 \quad (5)$$

where J_{wi} and J_{ww} ($L\ m^{-2}\ h^{-1}$) are the pure water fluxes of the membrane before and after BSA solution filtration, respectively. The flux loss was quantified using the total fouling ratio (R_t), described by:

$$R_t = R_r + R_{ir} = \left(1 - \frac{J_p}{J_{wi}}\right)100 \quad (6)$$

where R_r and R_{ir} are reversible and irreversible fouling, respectively. The reversible fouling is caused by concentration polarization and the formation of a gel layer on the membrane surface, and it can be cleaned (reversed) by distilled water washing. However, the irreversible fouling is caused by adsorption on the surface of membrane pores; it cannot be reversed by distilled water washing, and hence chemical washing is needed to clean the membrane [34]. R_r and R_{ir} were calculated using:

$$R_r = \left(\frac{J_{ww} - J_p}{J_{wi}}\right)100 \quad (7)$$

$$R_{ir} = \left(\frac{J_{wi} - J_{ww}}{J_{wi}}\right)100 \quad (8)$$

where J_p ($L\ m^{-2}\ h^{-1}$) is the BSA solution flux of the membrane.

3. Results and discussion

3.1. Characterization of salicylate-alumoxane nanoparticles

A TEM micrograph of the synthesized SA nanoparticles is depicted in Fig. 2; it shows the morphology of the nanoparticles

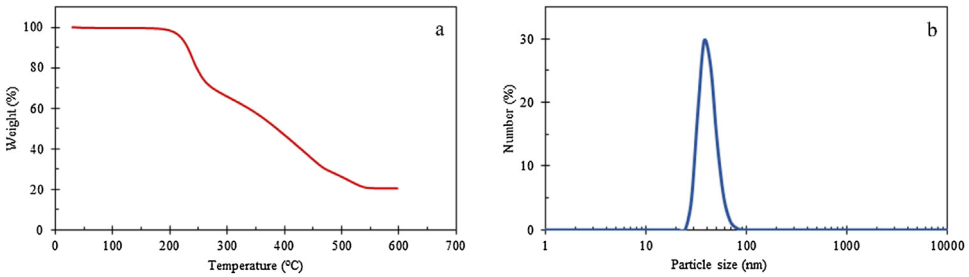

Fig. 3. (a) TGA thermogram and (b) particle size distribution of the SA nanoparticles.

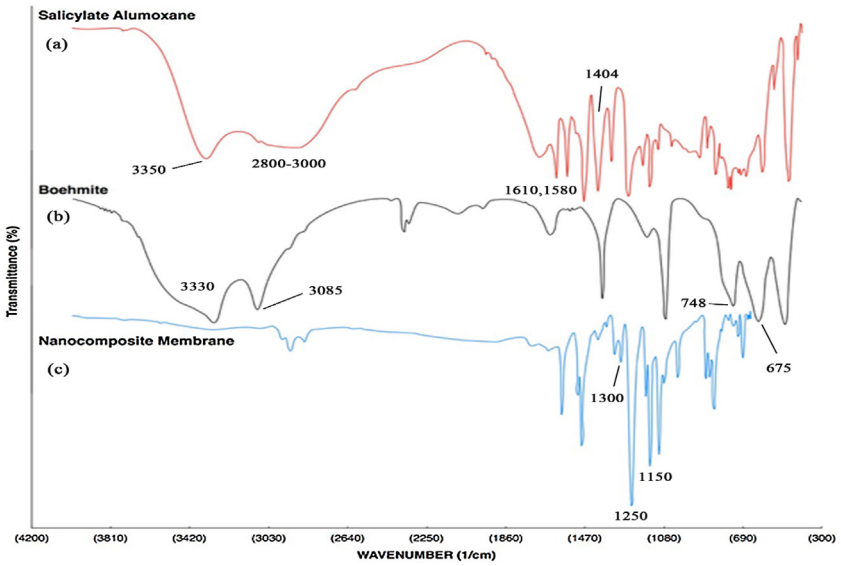

Fig. 4. FTIR spectra of (a) synthesized SA nanoparticle, (b) boehmite and (c) ATR-IR spectra of UF-S1 nanocomposite membrane.

at nanoscale. As can be seen, the width of these nanoparticles is about 75 nm.

The thermal stability of salicylate-alumoxane was studied via thermogravimetric analysis. Fig. 3(a) shows the TGA results. SA is thermally stable up to 220 °C. Beyond this temperature, its thermal degradation has two main steps. The first step with a 30.8 wt.% weight loss corresponds to the thermal degradation of salicylate organic structure. After phase transfer to alumina, the second step occurs at temperatures from 400 to 550 °C, ending with a salicylate-alumoxane residual weight of about 20.5%.

To measure the size and size distribution of the synthesized SA nanoparticles, dynamic light scattering (DLS) was used. A sample DLS result is shown in Fig. 3(b). As can be seen, the average diameter of 100 randomly-selected SA nanoparticles is about 49 nm. The SA nanoparticle average-diameter of less than 50 nm proves that the nanoscale-particle preparation was successful. DLS is a useful method for determining the agglomeration of nanoparticles in a solution. When nanoparticles are agglomerated, they have a polydispersity index (PDI) higher than 0.7. On the other hand, a PDI less than 0.1 indicates that the sample is highly monodisperse [39]. The small PDI value of 0.074 implies that these nanoparticles were well dispersed in the casting solution without any agglomeration.

The FTIR spectrum of boehmite nanoparticles is shown in Fig. 4b. The absorption peaks around 3085 cm^{-1} and 3330 cm^{-1} correspond to energy absorbed due to OH–Al bonds stretching. The absorption band at 1384 cm^{-1} is the stretch vibration of the nitrate. The peaks at 1072 cm^{-1} and 1163 cm^{-1} correspond to the symmetrical bending vibration of hydrogen bonds OH···OH. The two absorption peaks at 675 cm^{-1} and 748 cm^{-1} correspond to Al-O-Al bonds vibrations. These absorption peaks indicate that boehmite nanoparticles were successfully prepared. In FTIR spectrum of the SA nanoparticles (Fig. 4a), two absorption peaks at 675 cm^{-1} and 748 cm^{-1} correspond to the vibrations of Al—O—Al bonds. The peaks at 1145 cm^{-1} and 1255 cm^{-1} are due to the stretching vibrations of the carboxylate C—O and phenolic C—O groups, respectively. The two strong peaks at 1404 cm^{-1} and 1558 cm^{-1} correspond to the symmetrical and asymmetrical stretch vibrations of carbonyl groups of the carboxylate, respectively. The absorption peaks at 1475 cm^{-1} and 1610 cm^{-1} are assigned to C=C vibration of the benzene rings. The absorption peaks at 3030 cm^{-1} and 3075 cm^{-1} are assigned to the stretch vibrations of the aromatic C—H groups. Finally, the absorption peak appearing around 3335 cm^{-1} corresponds to phenolic OH groups. These absorption peaks indicate that SA nanoparticles were successfully prepared [36].

3.2. Characterization of nanocomposite membranes

3.2.1. ATR-FTIR analysis

The ATR-FTIR spectrum of the PS/SA nanocomposite membrane (UF-S1) is also shown in Fig. 4c. The ATR-FTIR spectrum of UF-S1 membrane shows peaks around 1151 cm^{-1}, 1300 cm^{-1} and 1250 cm^{-1}, which correspond to the symmetric and asymmetric stretch of O=S=O and the stretching vibration of C—O—C, respectively [23]. Also, the absorption peaks at 675 cm^{-1} and 748 cm^{-1} (vibrations of Al—O—Al bonds) and two strong peaks at 1404 cm^{-1} and 1558 cm^{-1} (vibrations of carbonyl groups of the carboxylate) confirm the presence of SA nanoparticles in the nanocomposite membrane.

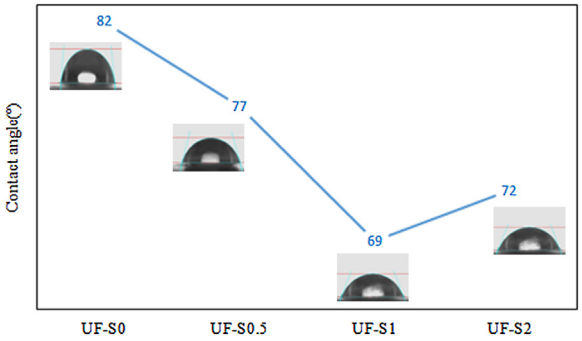

Fig. 5. Static contact angle (°) of water droplets on the surface of the prepared membranes.

3.2.2. Contact angle measurement

The tendency of water to wet a membrane surface is determined by the hydrophilicity parameter of the membrane, which is generally expressed in terms of contact angle. The contact angles of the synthesized membrane surfaces can be seen in Fig. 5. Contact angle of the neat PS membrane is relatively high ($82 \pm 0.5^{\circ}$), which is indicative of the low hydrophilicity of this membrane. The contact angle of the PS membrane decreased with the addition of SA to the PS casting solution up to 1 wt.% as observed for UF-S0.5 and UF-S1 membranes. The decrease in the contact angle indicates that the SA nanoparticles can improve the hydrophilicity of the PS membranes through the presence of extra hydroxyl groups on their surface [34]. However, by embedding 2 wt.% of SA nanoparticles, the contact angle of the modified membrane increased slightly ($72 \pm 0.2^{\circ}$) when compared to UF-S1 membrane. This can be due to higher agglomeration tendency of SA nanoparticles at high loading rate, which creates a rough surface for the membrane.

3.2.3. Membrane structure and surface morphologies

The FESEM images of cross-sections of the neat and nanocomposite membrane loaded with SA nanoparticles are shown in Fig. 6. As can be seen, all of the prepared membranes have a typical porous and asymmetric structure consisting of a thin top layer as a selective layer, a thick porous sub-layer with finger-like pores, and a macro-pores structure at the bottom of membrane, which is responsible for membrane mechanical support. The addition of SA nanoparticles as a hydrophilic additive influences the kinetic and thermodynamic aspects of the phase-separation process leading to the formation of various morphologies. Some researchers [40] believe that when an additive has a higher affinity to a non-solvent like water, finger-like structures are elongated due to a quicker liquid–liquid phase separation. The SA nanoparticles have good affinity to water due to their high hydrophilicity; the addition of SA to the casting solution decreases the thermodynamic stability of the non-solvent bath. Thus, the system becomes less stable and promotes a rapid exchange between the solvent and the non-solvent in the gelation bath during phase separation process. Therefore, the connectivity of the finger-like pores increases and narrow finger-like pores are formed across the cross-section of membrane [41]. However, a membrane with a thick top selective layer and a less

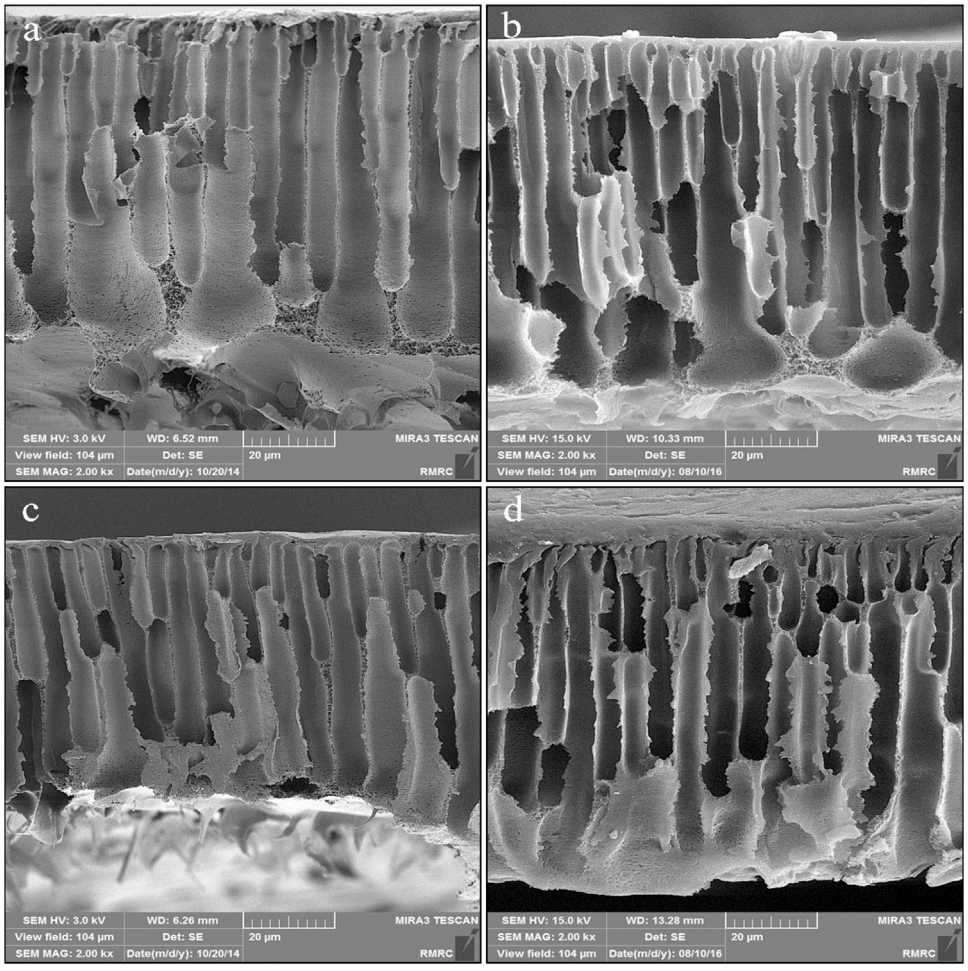

Fig. 6. The cross-section FESEM images of (a) neat membrane, (b) UF-S0.5, (c) UF-S1 and (d) UF-S2 nanocomposite membrane.

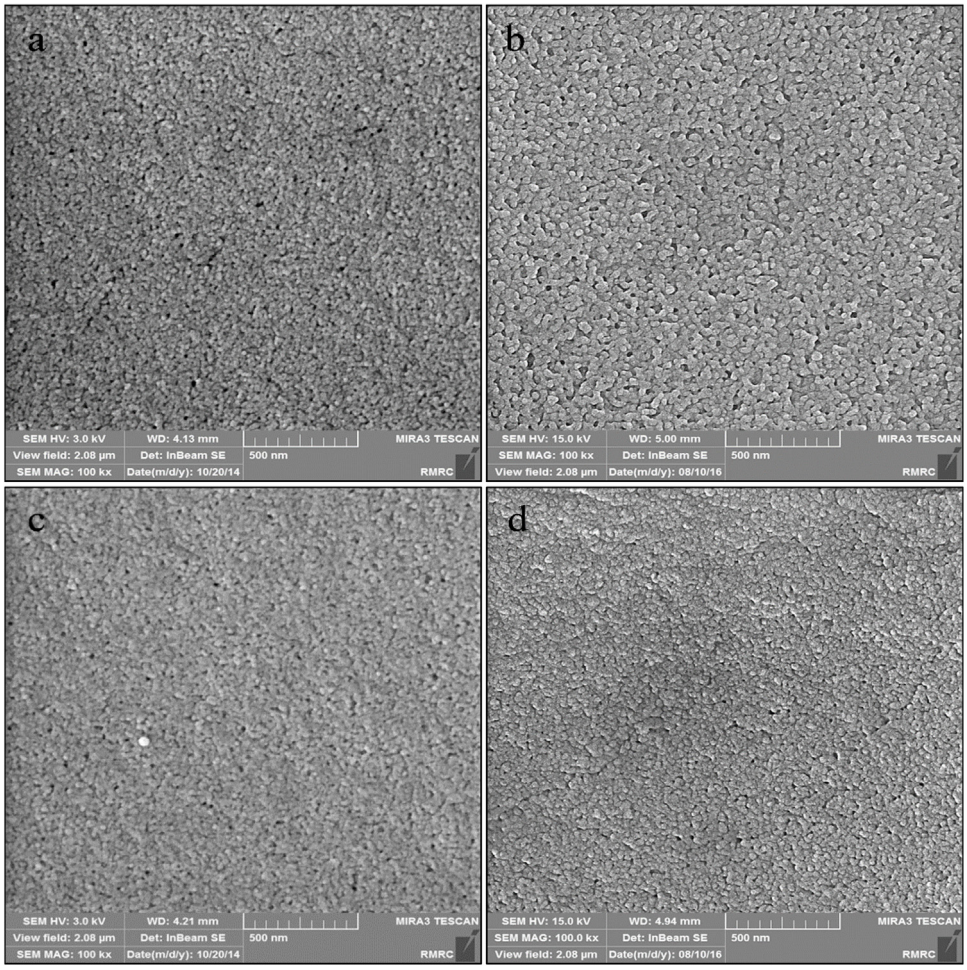

Fig. 7. Surface FESEM images of (b) UF-S0.5 and (d) UF-S2 nanocomposite membranes.

Table 1
Surface roughness parameters, overall porosities, and mean pore sizes of the prepared membranes.

membranes	S_a (nm)	S_q (nm)	S_z (nm)	Porosity (%)	Mean Pore size (nm)
UF-S0	18 ± 1.3	23.2 ± 1.7	186.48 ± 25.3	72	16.7
UF-S0.5	12.3 ± 0.8	16.3 ± 0.9	102.3 ± 14.2	77	13.8
UF-S1	5.3 ± 0.5	6.8 ± 0.7	52.3 ± 10.4	80	15.2
UF-S2	8.9 ± 0.4	11.3 ± 0.6	86.9 ± 12.5	76	12.6

porous support layer was formed when the SA content increased to 2 wt.%, (Fig. 6d). This can be explained by the delayed exchange of solvent and non-solvent in the phase-separation process due to the formation of a high viscous casting solution.

Top surface micrographs of the neat and modified PS membranes were also evaluated using a FESEM; sample results are shown in Fig. 7. As can be seen in Fig. 7(a), the neat membrane has relatively small pores on uniform surfaces that were formed during the membrane preparation. When SA nanoparticles were added to the casting solution, similar surfaces with small-size pores was formed. The mean pore size calculated from the permeation experiments confirmed the smaller pore size of the modified membranes (Table 1). As shown in Fig. 7(d), the membrane prepared with 2 wt.% SA possesses a denser surface due to the increased viscosity of the casting solution caused by the higher concentration of nanoparticles. In addition, from the FESEM images, it can be seen clearly that the SA nanoparticles were successfully embedded into the polymer matrix, and a homogeneous distribution without considerable agglomeration was achieved for the SA nanoparticles. This may be due to good affinity between SA and the polymer matrix.

Fig. 8 shows top surface EDAX spectra of the neat and the fabricated MMMs. Carbon, oxygen and sulfur peaks are seen in all graphs, but the aluminum peak exists only in the MMMs, which confirms the presence of nanoparticles in the MMMs. As can be seen in Fig. 8, the aluminum content increased, as the concentration of SA in the modified membranes increased. Also, the EDS mapping was performed to verify the distribution of SA nanoparticles on the UF-S2 membrane surface. The presence of elemental Al (red spots) indicates that the SA nanoparticles dispersed homogeneously on the MMM surfaces without any large agglomeration.

Two- and three-dimensional AFM images of the top surfaces of the neat and MMMs are shown in Fig. 9. The roughness parameters of the prepared membranes calculated from AFM images are given in Table 1. As can be seen, with the addition of SA nanoparticles the surfaces of MMMs became smoother than that of the PS membrane. The mean roughness (Sa) of the neat PS membrane gradually decreased from 18 ± 1.3 to 12.3 ± 0.8 nm and 5.3 ± 0.5 nm (Sa of the UF-S0.5 and UF-S1 membranes, respectively), and then increased to 8.9 ± 0.4 nm (Sa of the UF-S2 membrane). However, the UF-S2 membrane had a smoother surface than the PS membrane. The roughness increase of the membrane containing 2 wt.% SA is directly attributed to the accumulation of the SA nanoparticles on the membrane surface.

On the other hand, the protein molecules seem to be absorbed to the surfaces of the valleys of the membranes that have rough sur-

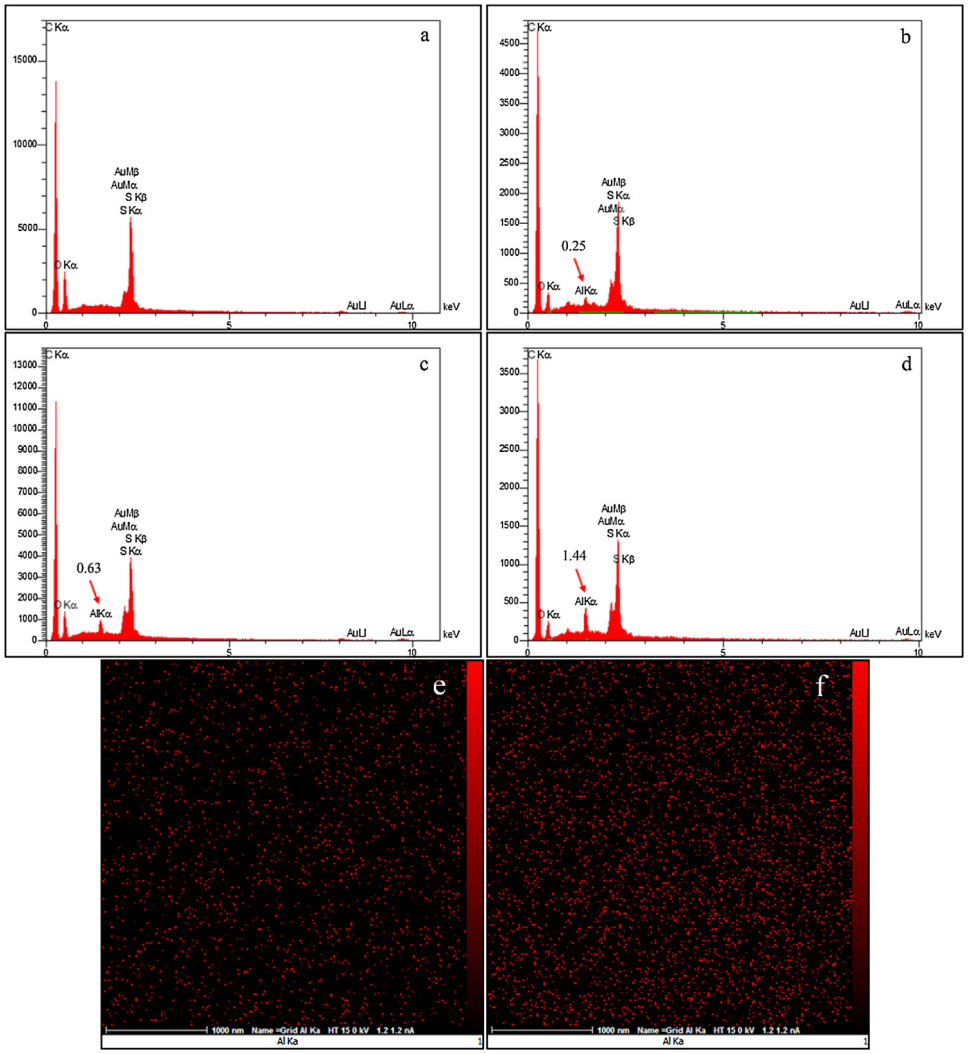

Fig. 8. EDAX spectra of the top surfaces of the fabricated membranes: (a) neat PS, (b) UF-S0.5, (c) UF-S1, and (d) UF-S2; and EDS mapping image of Al elemental distribution on the surface of (e) UF-S1 and (b) UF-S2.

faces [42]. This further confirms that a membrane with a smoother surface has better antifouling properties.

The overall porosities of the prepared membranes are given in Table 1. These results indicate that the MMMs have higher porosities than the neat PS membrane. The hydrophilicity of SA facilitates the water penetration from non-solvent bath into the polymer matrix and consequently increases the absorption capacity of the MMMs [25]. However, the porosity of UF-S2 membrane decreased, which can be attributed to the nanoparticles agglomeration and pore clogging in the membrane structure.

3.3. Filtration performance

The pure water flux and BSA retention results of the prepared membranes are shown in Fig. 10. As this figure shows, the flux of pure water increases with the addition of SA nanoparticles up to 0.1 wt.% and then decreases slightly. The mixed-matrix membrane containing 0.1 wt.% SA has the highest pure water flux of 300 l m^{-2} h^{-1} due to the larger pore size. The incorporation of SA nanoparticles into the PS membrane matrix can improve the hydrophilicity, which results in higher permeation and water flux. On the other hand, the presence of SA nanoparticles leads to the development of the finger-like pores and the improvement of the connectivity of pores over of the membrane thickness. This decreases the membrane hydraulic resistance and consequently increases water flux of membranes. In addition, SA may absorb water and provide alternative transport pathways for water media through the membrane. When the SA content increases (especially more than 2%), the water flux decreases due to the agglomeration of nanoparticles in the membrane pores.

As Fig. 10 shows, the protein rejection of the membranes increased, as their SA content was increased to 1 wt.%, but the rejection decreased slightly with a further increase beyond 1 wt.%. These results can be explained as follows. With the addition of nanoparticles to the casting solution, the pore size and roughness of the membrane surface decrease, leading to higher protein rejections for the mixed-matrix membranes. With a further increase in the SA content to 2 wt.%, the protein rejection decreased slightly due to the agglomeration of nanoparticles and membrane surface roughness increased (Table 1). In general, it is believed that membrane rejection increases, as the smoothness of the membrane surface increases [17]

3.4. Antifouling ability of membranes

To evaluate the antifouling properties of the membranes, the membranes were tested for protein solution filtration. The results of this study are shown in Fig. 11. The protein solution flux for the

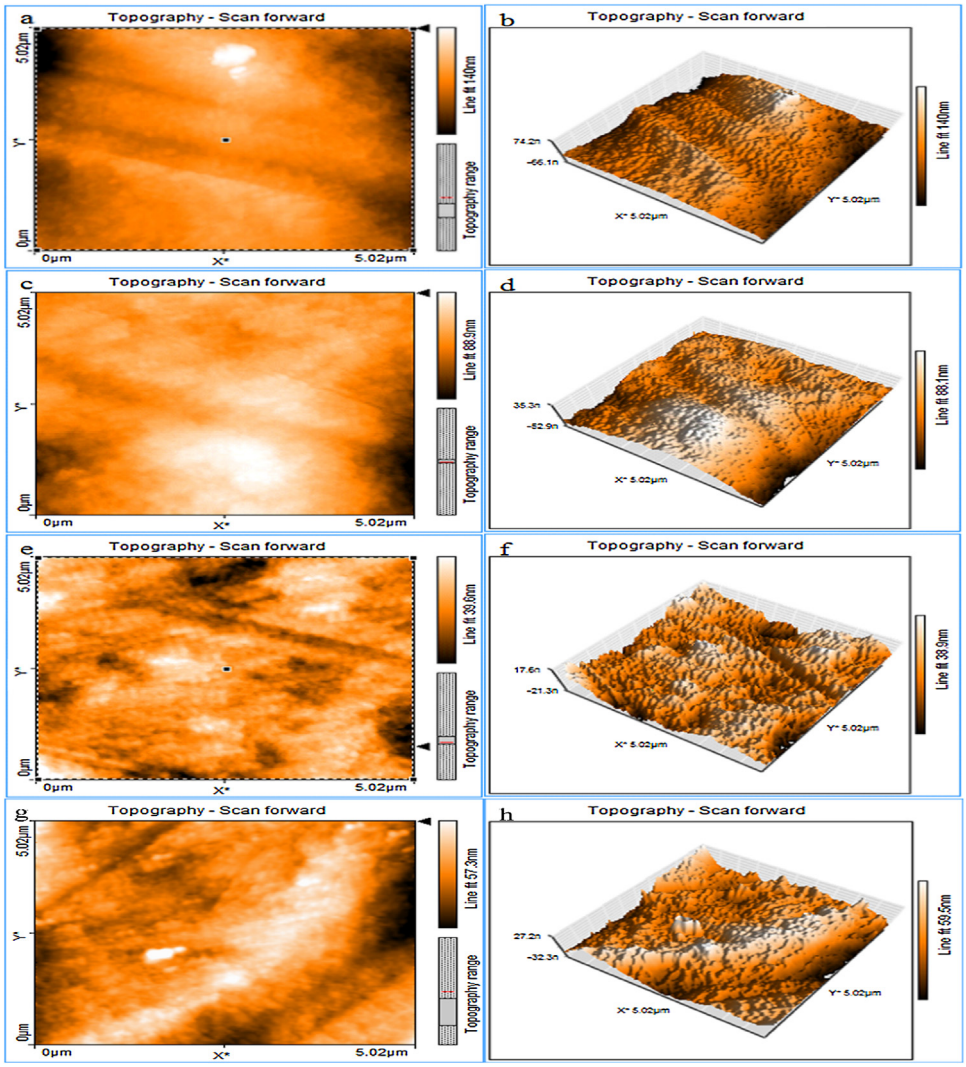

Fig. 9. Two- and three-dimensional AFM images of the top surfaces of the neat PS membrane (a and b), and UF-S0.5 (c and d), UF-S1 (e and f), and UF-S2 (g and h) nanocomposite membranes.

Table 2
Comparison of separation performance of present membranes with literature.

Membrane type	Pure water flux ($L\,m^{-2}\,h^{-1}$)	Protein flux ($L\,m^{-2}\,h^{-1}$)	Rejection (%)	FRR (%)	Refs.
2% Al_2O_3/PVDF	74.3	–	96.5	88.5	[44]
20% $TiSO_4$/CA	100.8	47	90.6	85.71	[45]
2% Silica/PES	180.2	75.8	96.1	76.2	[27]
10% $CaCO_3$/PS	–	–	94	71	[46]
1% SA/PS	210.1	147.95	99.3	87	This work

neat PS membrane is about $107\,l\,m^{-2}\,h^{-1}$ after 120 min. With the incorporation of the SA, the protein solution flux increased to 130, 134 and $143\,l\,m^{-2}\,h^{-1}$ for UF-S0.1, UF-S0.5 and UF-S1 membranes, respectively, and then decreased to $113.1\,l\,m^{-2}\,h^{-1}$ when the SA content increased to 2%. As can be seen in Fig. 11, at the beginning of the filtration, the fluxes of all of the prepared membranes decreased. This can be justified as follows. Some protein molecules in the feed solution were attached to the membrane surface and decreased the flux at the early stage of filtration. A steady-state flux is reached when the rate of the attachment of foulants to the surface and the rate of their release from the surface become equal [27]. As can be seen, the reduction in the protein solution flux of the neat membrane is higher than that of the hydrophilic composite membranes in the first 45 min before stabilizing due to the hydrophobic interaction between protein molecules and membrane surface [43]. In other words, the membranes modified by SA show a lower flux reduction and a higher steady-state flux. This can be explained as follows. The presence of SA and their hydrophilic centers on the surface and pores of membrane can reduce the hydrophobic interaction between BSA molecules and membrane surface and can inhibit the adsorption of protein molecules on the surface, and consequently can decrease the membrane fouling [33]. Although the 0.1 wt.% SA/PS membranes showed the highest pure-water flux, but the 1 wt.% SA/PS membranes had the highest protein-solution flux. The SA nanoparticles in the PS casting solution influence the membrane performance mainly through hydrophilicity and morphology. The highest pure-water flux of the UF-S0.1 membranes and the decline of the flux above 0.1 wt.% SA

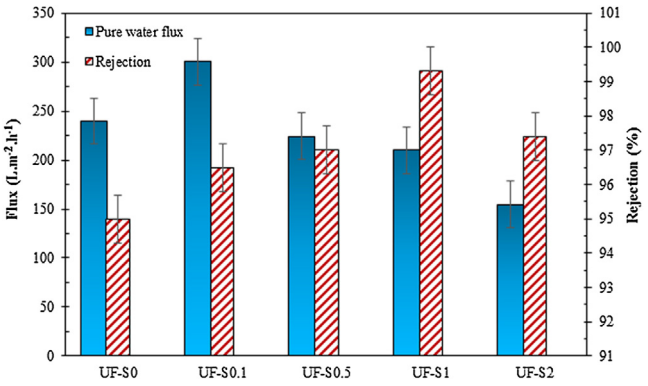

Fig. 10. Effects of SA concentration on pure water permeability and protein rejection of the membranes.

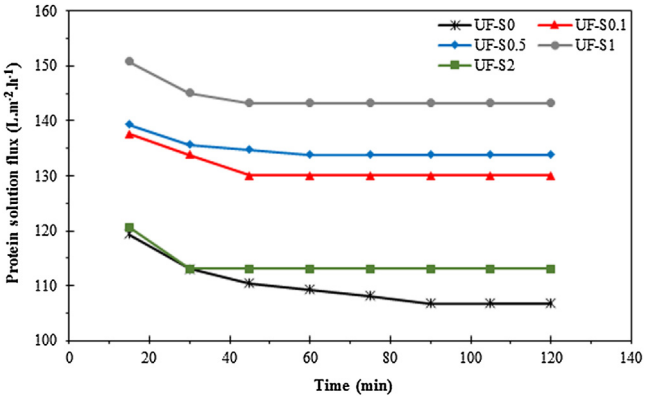

Fig. 11. Flux decline behavior of unmodified and modified membranes with different loading of SA during protein aqueous filtration.

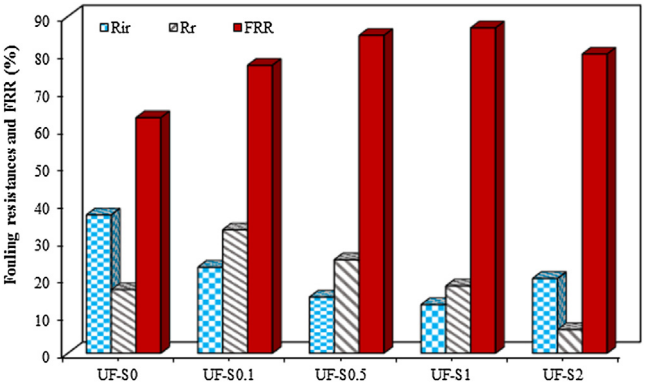

Fig. 12. Flux recovery ratios (*FRRs*) and fouling resistances of the membranes.

are ascribed to the change in membrane morphology. As suggested by Figs. 6 and 7, membranes with a dense top surface and a thick skin layer were formed when the concentration of SA in the casting solution was high. This implies that membrane morphology affects the pure-water flux more than hydrophilicity. On the other hand, the modified membranes with 1% wt. SA had smaller pore sizes and displayed better antifouling properties. These better antifouling properties can be attributed to the improvement of hydrophilicity and roughness, as the contact angle and AFM results indicate, respectively.

Important parameters for the evaluation of the antifouling properties of the fabricated membranes are the flux recovery ratio (*FRR*) and irreversible fouling (R_{ir}). A higher *FRR* and a lower R_{ir} are indicative of higher antifouling performance. Fig. 12 depicts the effect of the concentration of SA on *FRR* and R_{ir} of the neat and MMMs. The *FRR* value of the neat membrane is 63%, implying that serious fouling occurred on the neat membrane surface. The *FRR* increases to the maximum value of 87% with the addition of 1% SA to the casting solution, which indicates a good anti-fouling performance. The presence of SA on the surface of and inside the membrane can decrease the hydrophobic interaction between the membrane surface and protein molecules, and can inhibit the deposition of proteins on the membrane surface. When the SA content increases to 2%, *FRR* decreases, which can be due to pore blocking and agglomeration of the nanoparticles. The irreversible fouling decreases with the incorporation of SA nanoparticles to the casting solution, as shown in Fig. 12. R_{ir} value of the neat membrane is 37%, whereas this parameter decreases significantly to 13% for the 1% SA mixed-matrix membrane. As the nanoparticle content increases to 2 wt.% in the casting solution, pore blockage and agglomeration causes extra hydraulic resistance.

Table 2 compares the separation and antifouling performances of our best MMM with those of several membranes reported in the literature. It indicates that our MMMs have very good separation and antifouling performances.

4. Conclusions

To investigate the influence of SA nanoparticles on the morphology and performance of PS membranes, SA nanoparticles were synthesized and PS/SA nanocomposite ultrafiltration membranes were successfully fabricated via phase inversion induced by immersion precipitation. FTIR and EDAX analyses confirmed the presence of SA nanoparticles in the membrane structures. FESEM images showed that the addition of the nanoparticles reduces the sizes of the membrane surface and sub-layer pores, and increases the interconnectivity of the pores across the thickness of MMMs. The nanocomposite membranes have a higher hydrophilicity than neat PS membranes due to the presence of extra hydroxyl groups on the surface of SA nanoparticles. The ultrafiltration results showed that the water flux increases at low concentration of nanoparticles, and then decreases with a further increase in the nanoparticles concentration, due to the agglomeration of the nanoparticles in the membrane pores. Because of the reduction of the size of pores on the membrane surface, the protein rejection of the MMMs is higher. This study showed that the addition of SA nanoparticles to the PS casting solution improves the antifouling properties of PS membranes significantly.

Acknowledgment

The authors would like to thank Professor Mohsen Jahanshahi, the head of Nanotechnology Research Institute of Babol University of Technology, for his invaluable support.

References

[1] G. Romanos, C. Athanasekou, V. Likodimos, P. Aloupogiannis, P. Falaras, Hybrid ultrafiltration/photocatalytic membranes for efficient water treatment, Ind. Eng. Chem. Res. 52 (2013) 13938–13947.
[2] A. Rahimpour, S.S. Madaeni, S. Ghorbani, A. Shockravi, Y. Mansourpanah, The influence of sulfonated polyethersulfone (SPES) on surface nano-morphology and performance of polyethersulfone (PES) membrane, Appl. Surf. Sci. 256 (2010) 1825–1831.
[3] Y. Su, C. Mu, C. Li, Z. Jiang, Antifouling property of a weak polyelectrolyte membrane based on poly (acrylonitrile) during protein ultrafiltration, Ind. Eng. Chem. Res. 48 (2009) 3136–3141.
[4] K.P. Lee, D. Mattia, Monolithic nanoporous alumina membranes for ultrafiltration applications: characterization, selectivity-permeability analysis and fouling studies, J. Membr. Sci. 435 (2013) 52–61.
[5] B. Cancino-Madariaga, R. Ruby, C. Astudillo Castro, J. Saavedra Torrico, M. Lutz Riquelme, Analysis of the membrane fouling mechanisms involved in clarified

grape juice ultrafiltration using statistical tools, Ind. Eng. Chem. Res. 51 (2012) 4017–4024.
[6] P. Battistoni, E. Cola, F. Fatone, D. Bolzonella, A.L. Eusebi, Micropollutants removal and operating strategies in ultrafiltration membrane systems for municipal wastewater treatment: preliminary results, Ind. Eng. Chem. Res. 46 (2007) 6716–6723.
[7] E. Celik, L. Liu, H. Choi, Protein fouling behavior of carbon nanotube/polyethersulfone composite membranes during water filtration, Water Res. 45 (2011) 5287–5294.
[8] J. Liu, Y. Su, J. Peng, X. Zhao, Y. Zhang, Y. Dong, Z. Jiang, Preparation and performance of antifouling PVC/CPVC blend ultrafiltration membranes, Ind. Eng. Chem. Res. 51 (2012) 8308–8314.
[9] C.R. Kellenberger, N.A. Luechinger, A. Lamprou, M. Rossier, R.N. Grass, W.J. Stark, Soluble nanoparticles as removable pore templates for the preparation of polymer ultrafiltration membranes, J. Membr. Sci. 387 (2012) 76–82.
[10] E.M. Hoek, A.K. Ghosh, X. Huang, M. Liong, J.I. Zink, Physical–chemical properties, separation performance, and fouling resistance of mixed-matrix ultrafiltration membranes, Desalination 283 (2011) 89–99.
[11] S. Zhao, Z. Wang, X. Wei, B. Zhao, J. Wang, S. Yang, S. Wang, Performance improvement of polysulfone ultrafiltration membrane using well-dispersed polyaniline–poly (vinylpyrrolidone) nanocomposite as the additive, Ind. Eng. Chem. Res. 51 (2012) 4661–4672.
[12] A. Rahimpour, S.S. Madaeni, M. Jahanshahi, Y. Mansourpanah, N. Mortazavian, Development of high performance nano-porous polyethersulfone ultrafiltration membranes with hydrophilic surface and superior antifouling properties, Appl. Surf. Sci. 255 (2009) 9166–9173.
[13] S. Shenvi, A. Ismail, A.M. Isloor, Enhanced permeation performance of cellulose acetate ultrafiltration membranes by incorporation of sulfonated poly (1, 4-phenylene ether sulfone) and poly (styrene-co-maleic anhydride), Ind. Eng. Chem. Res. 53 (2014) 13820–13827.
[14] W. Ma, S. Rajabzadeh, H. Matsuyama, Preparation of antifouling poly (vinylidene fluoride) membranes via different coating methods using a zwitterionic copolymer, Appl. Surf. Sci. 357 (2015) 1388–1395.
[15] S. Yang, Z. Liu, Preparation and characterization of polyacrylonitrile ultrafiltration membranes, J. Membr. Sci. 222 (2003) 87–98.
[16] P.D. Peeva, T. Knoche, T. Pieper, M. Ulbricht, Cross-flow ultrafiltration of protein solutions through unmodified and surface functionalized polyethersulfone membranes – effect of process conditions on separation performance, Sep. Purif. Technol. 92 (2012) 83–92.
[17] T. Tweddle, O. Kutowy, W. Thayer, S. Sourirajan, Polysulfone ultrafiltration membranes, Ind. Eng. Chem. Prod. Res. Dev. 22 (1983) 320–326.
[18] H. Fan, C. Wang, Y. Li, Y. Wei, Preparation and anti-protein fouling property of δ-gluconolactone-modified hydrophilic polysulfone membranes, J. Membr. Sci. 415 (2012) 161–167.
[19] A. Rahimpour, S.S. Madaeni, Improvement of performance and surface properties of nano-porous polyethersulfone (PES) membrane using hydrophilic monomers as additives in the casting solution, J. Membr. Sci. 360 (2010) 371–379.
[20] S.B. Teli, S. Molina, A. Sotto, E.G.A. Calvo, J.D. Abajob, Fouling resistant polysulfone–PANI/TiO2 ultrafiltration nanocomposite membranes, Ind. Eng. Chem. Res. 52 (2013) 9470–9479.
[21] A. Rahimpour, S. Madaeni, A. Shockravi, S. Ghorbani, Preparation and characterization of hydrophile nano-porous polyethersulfone membranes using synthesized poly (sulfoxide-amide) as additive in the casting solution, J. Membr. Sci. 334 (2009) 64–73.
[22] J. Zhang, Z. Wang, X. Zhang, X. Zheng, Z. Wu, Enhanced antifouling behaviours of polyvinylidene fluoride membrane modified through blending with nano-TiO_2/polyethylene glycol mixture, Appl. Surf. Sci. 345 (2015) 418–427.
[23] F. Li, J. Ye, L. Yang, C. Deng, Q. Tian, B. Yang, Surface modification of ultrafiltration membranes by grafting glycine-functionalized pva based on polydopamine coatings, Appl. Surf. Sci. 345 (2015) 301–309.
[24] X. Zhang, W.-Z. Lang, X. Yan, Z.-Y. Lou, X.-F. Chen, Influences of the structure parameters of multi-walled carbon nanotubes (MWNTs) on PVDF/PFSA/O-MWNTs hollow fiber ultrafiltration membranes, J. Membr. Sci. 499 (2016) 179–190.
[25] H. Rabiee, M.H.D.A. Farahani, V. Vatanpour, Preparation and characterization of emulsion poly (vinyl chloride)(EPVC)/TiO_2 nanocomposite ultrafiltration membrane, J. Membr. Sci. 472 (2014) 185–193.
[26] S. Madaeni, N. Ghaemi, A. Alizadeh, M. Joshaghani, Influence of photo-induced superhydrophilicity of titanium dioxide nanoparticles on the anti-fouling performance of ultrafiltration membranes, Appl. Surf. Sci. 257 (2011) 6175–6180.
[27] J. Huang, K. Zhang, K. Wang, Z. Xie, B. Ladewig, H. Wang, Fabrication of polyethersulfone-mesoporous silica nanocomposite ultrafiltration membranes with antifouling properties, J. Membr. Sci. 423 (2012) 362–370.
[28] Z.-K. Li, W.-Z. Lang, W. Miao, X. Yan, Y.-J. Guo, Preparation and properties of PVDF/SiO_2@GO nanohybrid membranes via thermally induced phase separation method, J. Membr. Sci. 511 (2016) 151–161.
[29] Y.L. Thuyavan, N. Anantharaman, G. Arthanareeswaran, A. Ismail, Adsorptive removal of humic acid by zirconia embedded in a poly (ether sulfone) membrane, Ind. Eng. Chem. Res. 53 (2014) 11355–11364.
[30] J.-H. Li, X.-S. Shao, Q. Zhou, M.-Z. Li, Q.-Q. Zhang, The double effects of silver nanoparticles on the PVDF membrane: surface hydrophilicity and antifouling performance, Appl. Surf. Sci. 265 (2013) 663–670.
[31] F.Q. Mir, A. Shukla, Negative rejection of NaCl in ultrafiltration of aqueous solution of NaCl and KCl using sodalite octahydrate zeolite-clay charged ultrafiltration membrane, Ind. Eng. Chem. Res. 49 (2010) 6539–6546.
[32] A.V. Dudchenko, J. Rolf, K. Russell, W. Duan, D. Jassby, Organic fouling inhibition on electrically conducting carbon nanotube–polyvinyl alcohol composite ultrafiltration membranes, J. Membr. Sci. 468 (2014) 1–10.
[33] J. María Arsuaga, A. Sotto, G. del Rosario, A. Martínez, S. Molina, S.B. Teli, J. de Abajo, Influence of the type size, and distribution of metal oxide particles on the properties of nanocomposite ultrafiltration membranes, J. Membr. Sci. 428 (2013) 131–141.
[34] V. Vatanpour, S.S. Madaeni, L. Rajabi, S. Zinadini, A.A. Derakhshan, Boehmite nanoparticles as a new nanofiller for preparation of antifouling mixed matrix membranes, J. Membr. Sci. 401 (2012) 132–143.
[35] L. Rajabi, A. Derakhshan, Room temperature synthesis of boehmite and crystallization of nanoparticles: effect of concentration and ultrasound, Sci. Adv. Mater. 2 (2010) 163–172.
[36] A.A. Derakhshan, L. Rajabi, H. Karimnezhad, Morphology and production mechanism of the functionalized carboxylate alumoxane micro and nanostructures, Powder Technol. 225 (2012) 156–166.
[37] A.M. Alsari, K. Khulbe, T. Matsuura, The effect of sodium dodecyl sulfate solutions as gelation media on the formation of PES membranes, J. Membr. Sci. 188 (2001) 279–293.
[38] C. Feng, R. Wang, B. Shi, G. Li, Y. Wu, Factors affecting pore structure and performance of poly (vinylidene fluoride-co-hexafluoro propylene) asymmetric porous membrane, J. Membr. Sci. 277 (2006) 55–64.
[39] M. Kaszuba, D. McKnight, M.T. Connah, F.K. McNeil-Watson, U. Nobbmann, Measuring sub nanometre sizes using dynamic light scattering, J. Nanopart. Res. 10 (5) (2008) 823–829.
[40] A. Mollahosseini, A. Rahimpour, M. Jahamshahi, M. Peyravi, M. Khavarpour, The effect of silver nanoparticle size on performance and antibacteriality of polysulfone ultrafiltration membrane, Desalination 306 (2012) 41–50.
[41] H. Yu, X. Zhang, Y. Zhang, J. Liu, H. Zhang, Development of a hydrophilic PES ultrafiltration membrane containing SiO_2@N-Halamine nanoparticles with both organic antifouling and antibacterial properties, Desalination 326 (2013) 69–76.
[42] A. Razmjou, J. Mansouri, V. Chen, The effects of mechanical and chemical modification of TiO_2 nanoparticles on the surface chemistry, structure and fouling performance of PES ultrafiltration membranes, J. Membr. Sci. 378 (2011) 73–84.
[43] J.-N. Shen, H.-M. Ruan, L.-G. Wu, C.-J. Gao, Preparation and characterization of PES–SiO2 organic–inorganic composite ultrafiltration membrane for raw water pretreatment, Chem. Eng. J. 168 (2011) 1272–1278.
[44] L. Yan, Y.S. Li, C.B. Xiang, S. Xianda, Effect of nano-sized Al_2O_3-particle addition on PVDF ultrafiltration membrane performance, J. Membr. Sci. 276 (2006) 162–167.
[45] J. Dasgupta, S. Chakraborty, J. Sikder, R. Kumar, D. Pal, S. Curcio, E. Drioli, The effects of thermally stable titanium silicon oxide nanoparticles on structure and performance of cellulose acetate ultrafiltration membranes, Sep. Purif. Technol. 133 (2014) 55–68.
[46] A.K. Nair, A.M. Isloor, R. Kumar, A.F. Ismail, Antifouling and performance enhancement of polysulfone ultrafiltration membranes using $CaCO_3$ nanoparticles, Desalination 322 (2013) 69–75.